Phonons and lithium diffusion in $LiAlO_2$

Mayanak K. Gupta,[1,2,*] Ranjan Mittal,[1,3,†] Baltej Singh,[1,3] Olivier Delaire,[2] Srungarpu N. Achary,[3,4] Stephane Rols,[5]
Avesh K. Tyagi,[3,4] and Samrath L. Chaplot[1,3]
[1]*Solid State Physics Division, Bhabha Atomic Research Centre, Mumbai 400085, India*
[2]*Department of Mechanical Engineering and Materials Science, Duke University, Durham, North Carolina, USA*
[3]*Homi Bhabha National Institute, Anushaktinagar, Mumbai 400094, India*
[4]*Chemistry Division, Bhabha Atomic Research Centre, Mumbai 400085, India*
[5]*Institut Laue-Langevin, BP 156, 38042 Grenoble Cedex 9, France*

(Received 24 August 2020; accepted 3 May 2021; published 13 May 2021)

We report on investigations of phonons and lithium diffusion in $LiAlO_2$ based on inelastic neutron scattering measurements of the phonon density of states (DOS) in γ-$LiAlO_2$ from 473 to 1073 K, complemented with *ab initio* molecular dynamics (AIMD) simulations. We find that phonon modes related to Li vibrations broaden on warming as reflected in the measured phonon DOS and reproduced in simulations. Further, the AIMD simulations probe the nature of lithium diffusion in the perfect crystalline phase (γ-$LiAlO_2$), as well as in a structure with lithium vacancies and a related amorphous phase. In all three structures, almost liquidlike superionic diffusion is observed in AIMD simulations at high temperatures, with predicted onset temperatures of 1800, 1200, and 600 K in the perfect structure, vacancy structure, and the amorphous phase, respectively. In the ideal structure, the Li atoms show correlated jumps, while simple and correlated jumps are both seen in the vacancy structure, and a mix of jumps and continuous diffusion occurs in the amorphous structure. Further, we find that Li diffusion is facilitated in all cases by a large librational amplitude of the neighboring AlO_4 tetrahedra and that the amorphous structure opens additional diffusion pathways due to a broad distribution of AlO_4 tetrahedra orientations.

DOI: 10.1103/PhysRevB.103.174109

I. INTRODUCTION

Li-ion batteries are the backbone of present energy storage technology, including in countless portable electronic devices [1,2]. The shift away from organic liquids toward solid electrolytes represents an important milestone for the next generation of Li-ion batteries [3,4]. Many compounds (thiophosphates, sulphates, and oxides) were recently discovered to exhibit very high Li-ion conductivity, making them of interest as possible solid electrolytes [5–8]. Solid electrolytes could possibly enable the use of Li metal as anode, as well as high energy density cathodes. However, no solid electrolytes so far have been found suitable against Li metal as well as high voltage cathodes [9,10]. The electrode-solid electrolyte interfaces are observed to be chemically or electrochemically unstable and tend to react to form undesirable compounds [11–13]. These products may be good electronic conductors but with poor Li-ion conductivity and promote detrimental dendrite formation in the cell [14,15]. To avoid unnecessary chemical reactions at the interfaces, the electrodes can be coated with a suitable material exhibiting high Li-ion conductivity, high electronic bandgap, and good thermal and mechanical stability [16]. $LiAlO_2$ has been proposed as a suitable candidate for this application [17,18]. Moreover, Al-containing $LiCoO_2$, NCA ($LiNi_{0.8}Co_{0.15}Al_{0.05}O_2$), is popular as a cathode material for Li-ion batteries. Therefore, understanding the mechanism of Li diffusion in $LiAlO_2$ is important to find ways to enhance Li diffusion at lower temperatures to improve the design of future solid-state batteries.

The diffusion of lithium is considered as an important factor for the design, stability, and performance of $LiAlO_2$-based devices. In recent years, $LiAlO_2$ has been extensively studied, using a wide range of experimental and computational techniques [19–26], for its interesting properties as a Li-ion battery material. Phase transformations occurring in $LiAlO_2$ upon H adsorption have been investigated [27] using combined experimental and first-principles studies. $LiAlO_2$ is also an important material in the microelectronics industry. Because it exhibits fine-tunable lattice changes during lithium diffusion, it is suitable as a substrate material for epitaxial growth of III−V semiconductors like GaN [28]. Further, in the nuclear industry, $LiAlO_2$ is also considered a blanket material for the tritium breeder in nuclear fusion reactors [29,30]. Classical molecular dynamics (MD) simulations suggest [31] that tritium migration is promoted and controlled by lithium diffusion. The radiation damage process in $LiAlO_2$ has also been studied [32] on an atomic scale using classical MD simulations.

Six polymorphs of $LiAlO_2$ are reported in the literature [21,27,33–35]. However, the structures of only four of these (α, β, γ, and δ) are known [35]. The γ-$LiAlO_2$ is the only stable phase under ambient conditions. The structure of

---

[*] mayankg@barc.gov.in
[†] rmittal@barc.gov.in

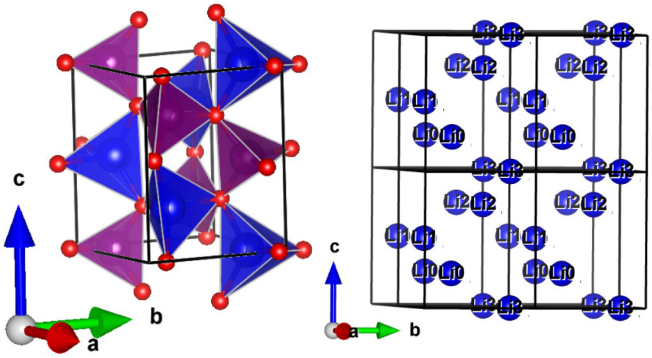

FIG. 1. (Left) The crystal structure of γ-LiAlO$_2$. Red, blue, and violet spheres represent the oxygen, lithium, and aluminium atoms, respectively, at their lattice sites. The polyhedral units around Li and Al are shown in blue and violet, respectively. (Right) Lithium atoms in a supercell of 2 × 2 × 2. Li0, Li1, Li2, and Li3 correspond to the four lithium atoms in the unit cell of γ-LiAlO$_2$.

γ-LiAlO$_2$ (Fig. 1, tetragonal space group $P4_12_12$, $Z = 4$) has been investigated using neutron and x-ray diffraction (XRD) techniques [20,33]. The structure consists of AlO$_4$ and LiO$_4$ polyhedral units sharing an edge. The γ phase is stable [36] up to 1873 K. The temperature dependence of zone-center Raman active modes has been reported in γ-LiAlO$_2$ from 78 to 873 K, which showed a considerable broadening of the phonon modes involving Li vibrations [25]. The dynamics of Li ions in a LiAlO$_2$ single crystal has been studied by nuclear magnetic resonance (NMR) spectroscopy and conductivity measurements, from which a Li activation energy ~1.14 eV and a diffusion coefficient $\sim 10^{-13}\ \mathrm{m^2/s}$ were estimated at 1000 K [26]. However, the diffusion pathway for Li could not be determined from these NMR and conductivity measurements [26], but it was speculated that Li jump diffusion proceeds between tetrahedral sites via an intermediate octahedral site [26]. Another investigation of Li diffusion based on high-temperature neutron diffraction, tracer diffusion, and conductivity spectroscopy experiments estimated the Li activation energy to be ~0.72 and ~1.0–1.2 eV for powder and single-crystal samples, respectively [20,21]. The authors explained the difference in barrier energy between these two forms of the compound with the presence in larger concentrations of defects and vacancies in the powder sample than in the single crystal. A study in amorphous LiAlO$_2$ from room temperature and 473 K showed [37] that the lithium diffusivity obeys the Arrhenius law with an activation energy of 0.94 eV and significantly higher Li diffusion coefficient $3.6 \times 10^{-15}\ \mathrm{m^2/s}$ at 473 K, which is three orders of magnitude higher than in crystalline phase ($\sim 10^{-18}\ \mathrm{m^2/s}$) at the same temperature [26]. A study on disordered γ-LiAlO$_2$ showed that the introduction of structural disorder significantly enhances the Li ion conductivity in γ-LiAlO$_2$ [24].

Several solid superionic electrolytes have been discovered in which the diffusion mechanism is found to be strongly correlated with the rotational dynamics of constituent polyhedra [38]. We earlier performed [39] extensive *ab initio* calculations of phonons, high-pressure phase stability, and thermal expansion behavior in different phases of LiAlO$_2$. We have also investigated the thermodynamic and ionic transport properties in several Li- and Na-based solid-ionic conductors using *ab initio* molecular dynamics (AIMD) simulations and neutron scattering measurements [40–44]. Here, we focus on the diffusion mechanism of Li in various phases of LiAlO$_2$ and the structural and dynamical features relevant to Li diffusion. The compound LiAlO$_2$ exhibits a simple framework structure in its γ phase, where the AlO$_4$ polyhedral units form a three-dimensional network connected via terminal oxygen, and the Li atoms occupy the octahedral voids formed between these tetrahedral units. The ionic conductivity in the perfect crystalline structure is very limited [20,22]. However, the amorphous phase exhibits significantly higher ionic conductivity [37]. Thus, we are asking two main questions: (i) Does the activation of AlO$_4$ rotation lead to Li diffusion in the crystalline phase? (ii) How does amorphization promote Li diffusion? To address these questions, we performed AIMD simulations for both the crystalline and amorphous structures. Further, we also investigated the role of Li vacancies in promoting ionic diffusion. Phonons are important, as they dynamically modulate the structure and hence may affect the diffusion jumps. Thus, it is interesting to investigate the behavior of phonon spectra as a function of temperature and examine their possible correlation with Li diffusion. We have measured the temperature dependence of phonon spectra in γ-LiAlO$_2$ up to 1073 K, and the observed spectral changes are interpreted based on our AIMD simulations.

II. EXPERIMENTAL

A polycrystalline sample of γ-LiAlO$_2$ was prepared [33] by solid-state reaction of Li$_2$CO$_3$ and γ-Al$_2$O$_3$. Here, γ-Al$_2$O$_3$ was heated at 700 °C overnight before use. Desired amounts of Li$_2$CO$_3$ and preheated γ-Al$_2$O$_3$ in 1.01:1.00 molar ratio were mixed thoroughly and pressed into pellets of 20 mm diameter and 10 mm height. A slight excess of Li$_2$CO$_3$ was employed to compensate for the loss of Li$_2$CO$_3$ at high temperatures. The pellets were heated at 600 °C for 12 h and then crushed to powder and repelletized. These pellets were again heated at 800 °C for 24 h, and then the temperature was raised to 950 °C and held for 24 h. The bright white pellets were crushed to powder and characterized by powder XRD. The formation of phase pure tetragonal γ-LiAlO$_2$ was confirmed by comparing the XRD data with that reported in the literature [20,21].

The inelastic neutron scattering (INS) measurements of the phonon density of states (DOS) on the γ-phase of LiAlO$_2$ were carried out using the time-of-flight spectrometer IN4C at the Institut Laue Langevin, France. Thermal neutrons of wavelength 2.4 Å (14.2 meV) were used for the measurements, which were performed in neutron energy gain mode. We used $2\ \mathrm{cm^3}$ of the polycrystalline sample of γ phase of LiAlO$_2$ for the measurements. The polycrystalline sample was loaded inside an 8-mm-diameter cylindrical can of niobium. The data from the sample and empty niobium can were collected at several temperatures from 473 to 1073 K. The detector bank at IN4C covered a wide range scattering angle from10 ° to 110 °. The data analysis was carried out in the incoherent one-phonon approximation to extract the DOS. In this approximation, the measured scattering function $S(Q,E)$, where E and Q are the energy transfer and momentum transfer vector, respectively, is related [45–47] to the neutron-weighted phonon DOS $g^{(n)}(E)$ as follows:

$$g^{(n)}(E) = A\left\langle \frac{e^{2W(Q)}}{Q^2}\frac{E}{n(E,T)+\frac{1}{2}\pm\frac{1}{2}}S(Q,E)\right\rangle, \tag{1}$$

$$g^{(n)}(E) = B\sum_k \left\{\frac{4\pi b_k^2}{m_k}\right\} g_k(E), \tag{2}$$

where the + or – signs correspond to the energy loss or gain of the neutrons, respectively, $n(E,T) = [\exp(E/k_BT) - 1]^{-1}$, T is temperature and k_B the Boltzmann's constant. Here, A and B are normalization constants and b_k, m_k, and $g_k(E)$ are, respectively, the neutron scattering length, mass, and partial DOS of the kth atom in the unit cell. The quantity between ⟨⟩ represents a suitable average over all Q values at a given energy. Here, $2W(Q)$ is the Debye-Waller factor averaged over all the atoms. The weighting factors $\frac{4\pi b_k^2}{m_k}$ for various atoms in the units of barns/amu are 0.1974, 0.2645, and 0.0557 for Li, O, and Al, respectively. The values of neutron scattering lengths for various atoms can be found in Ref. [48].

III. COMPUTATIONAL DETAILS

The AIMD simulations were performed at several temperatures (>300–2200 K) using the VASP software [49,50]. The simulations used a 2 × 2 × 2 supercell (128 atoms) of the ambient phase structure of γ-LiAlO$_2$ and were performed for three cases: the ideal crystalline phase, a defect structure with one Li vacancy out of the 32 Li positions in the 128 atoms supercell, and in an approximant of the amorphous phase. Since the AIMD simulations are computationally expensive, we used a single electronic k-point at Γ point for the total energy calculations. The calculations used the projector augmented wave density functional theory formalism within the generalized gradient approximation parameterization by Perdew, Becke, and Ernzerhof [51–53]. A plane-wave kinetic energy cutoff of 820 eV and an energy convergence criterion of 10^{-6} eV were used. The time step was 2 fs in all simulations. All simulations were performed for ~90 ps using a moles, volume, temperature (NVT) ensemble with a Nosé thermostat [54]. We have shown in Fig. S1 (Supplemental Material [55]) the temperature and total-energy profiles during the NVT simulations, which indicate a negligible drift in these values. The first 10 ps simulation data were considered for equilibration, and next, 80 ps simulation data were used for production. For the simulations at high temperatures, we have used a larger volume than that at 0 K to account for the thermal expansion, as estimated from the experimental data [21] as well as previously reported *ab initio* calculations [39]. Typically, the volume expansion is ~5.7% at 1700 K.

We note that the melting point of LiAlO$_2$ [56] is ~1873 K, which is comparable with the highest temperature we have simulated for a perfect crystal. However, melting being a first-order transition involves a large energy barrier. As our simulations are performed for ~90 ps in an NVT ensemble, we do not expect to observe melting at the experimental melting point. Melting would occur in the simulations at somewhat higher temperature. To create the amorphous phase, we started with the crystalline structure of γ-LiAlO$_2$ with 128 atoms. The crystalline phase was melted at 5000 K for 10 ps. Then the melted structure was quenched to 10 K, which was further used in the simulations in the amorphous phase at various temperatures from 300 to 1400 K.

The vibrational DOS from AIMD simulations was obtained [57] via a Fourier transform of the velocity autocorrelation function (VACF). The simulations performed up to 60 ps give an energy resolution of ~0.1 meV in the calculation of the phonon DOS, exceeding the experimental energy resolution (~1 to 10 meV with ~10% of the energy transfer). The time-averaged pair-distribution function (PDF) of various pairs of atoms in crystalline, vacancy structure, and amorphous phase of γ-LiAlO$_2$ has been calculated using the following relation [58]:

$$g_{IJ}(r) = \frac{n_{IJ}(r)}{\rho_J 4\pi r^2 dr}, \tag{3}$$

where $n_{IJ}(r)$ is the average number of atoms of species J in a shell of width dr at distance r from an atom of species I, and ρ_J is the average number density of the species J. We have also computed the self [$g_s(r,t)$] and distinct [$g_d(r,t)$] Van Hove correlation functions [59] to investigate the self and correlated diffusion in various structures. The diffusion process can be investigated in AIMD simulations by monitoring the trajectories and the time dependence of the atomic mean-squared displacement (MSD) of different atom types. The time dependence of MSD is related to the isotropic diffusion coefficient [60] by the relation

$$D = \frac{\langle u^2\rangle}{6\tau}, \tag{4}$$

where $\langle u^2\rangle$ is the MSD at time τ and is calculated using well-known numerical methods [57,61]. We have also calculated the diffusion coefficient using the VACF [62].

IV. RESULTS AND DISCUSSION

A. Temperature dependence of phonon spectra

The temperature-dependent DOS measured with INS from 473 to 1073 K is shown in Fig. 2(a). The peaks at ~20, 22, 30, 35, 40, 45, 60, and 95 meV are clearly getting broadened on warming. The broadening is particularly prominent at temperatures of 873 K and above, at which point the peak structure is suppressed. The broadening may be due to the onset of significant diffusion of Li atoms. The observed evolution of the DOS at high temperature was compared with the DOS from AIMD simulations (Fig. 2), which incorporates anharmonic effects [63]. The experimental DOS at 473 K is compared with the AIMD calculations at 300 K [Fig. 2(b)]. The calculated phonon DOS reproduces [Fig. 2(b)] the overall shape and peak positions in the experimental DOS. We regard the agreement between the experimental and calculation as fair, considering the known inherent approximations both in the experiment (e.g., incoherent approximation for the intensities and multiphonon contribution) and theory (e.g., limited wave-vector mesh due to a small AIMD simulation cell).

Further, we isolate the contribution of different atomic species to the INS spectra by computing the partial DOS from AIMD trajectories (Fig. 3). As can be seen in this figure, the Li contribution to the DOS extends up to 80 meV, while O

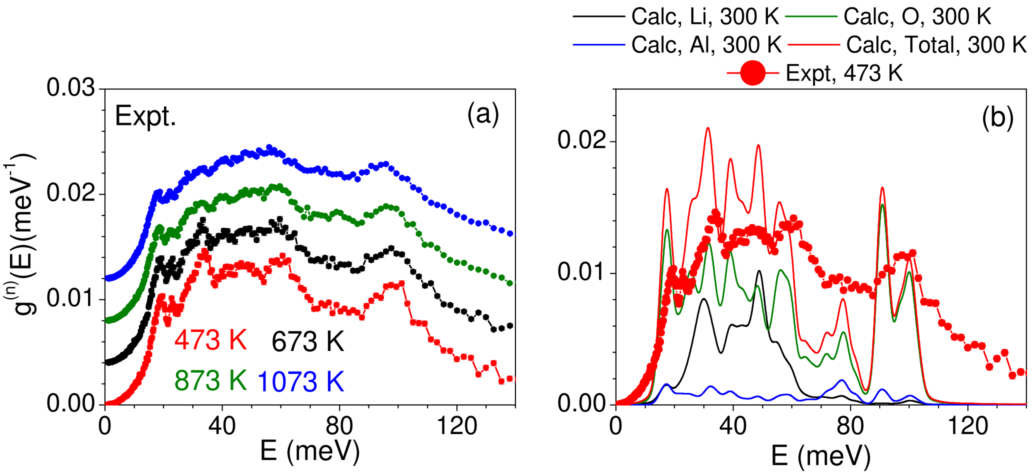

FIG. 2. (a) The experimentally measured phonon density of states (DOS) in γ-LiAlO$_2$ at various temperatures obtained using inelastic neutron scattering measurements. (b) Experimental (473 K) and *ab initio* molecular dynamics (AIMD) calculated (300 K) neutron-weighted phonon DOS. The calculated partial contributions from various atoms are also shown.

and Al contribute to the entire spectral range up to 110 meV. The sharp peaklike structure in the Li partial DOS at 300 K broadens significantly on warming and becomes suppressed at 2200 K. We also observed a significant broadening of the Al and O partial DOS; however, the peak structure in the DOS is retained. The large broadening and loss of peak structure in the Li partial DOS can be described as follows. The Li atoms are located at equilibrium sites in the crystalline structure and metastable sites in the amorphous structure. From the fact that the Li atoms show diffusion, it may be expected that they are

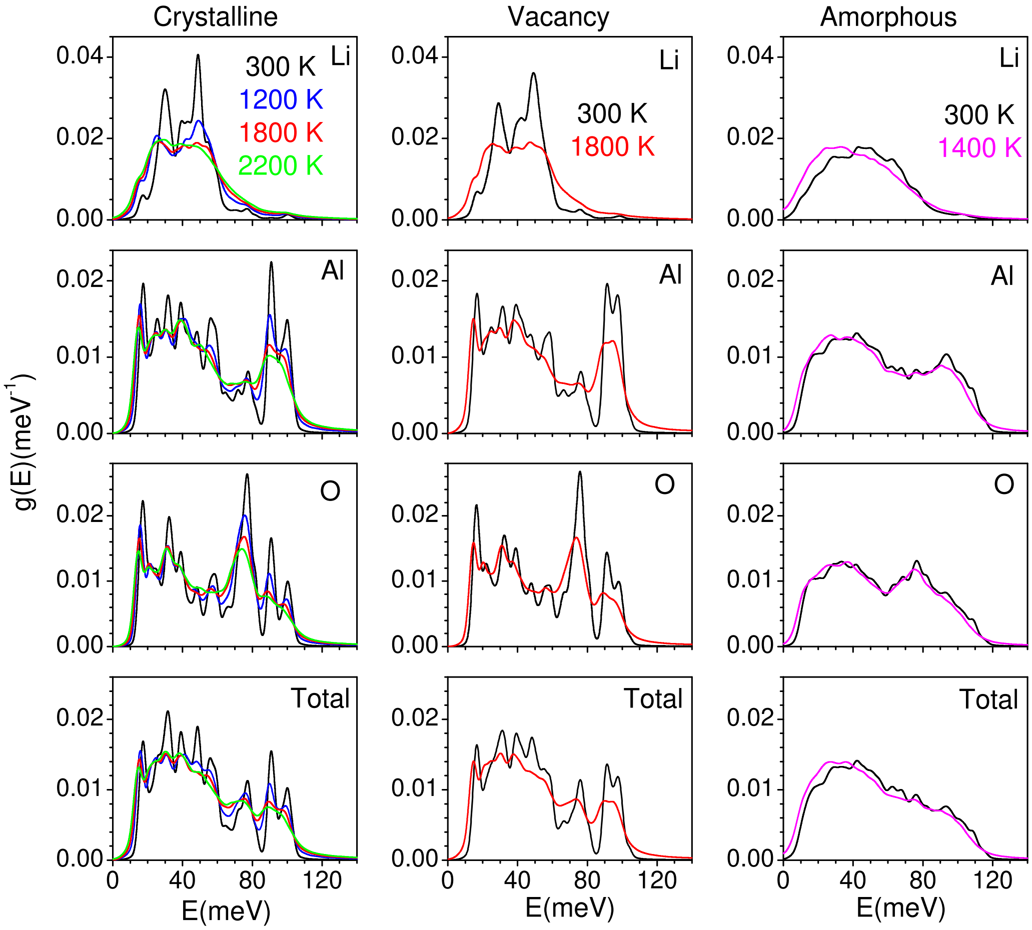

FIG. 3. The *ab initio* molecular dynamics (AIMD) calculated partial and total phonon density of states in the perfect crystalline phase, vacancy structure, and amorphous phase of γ-LiAlO$_2$.

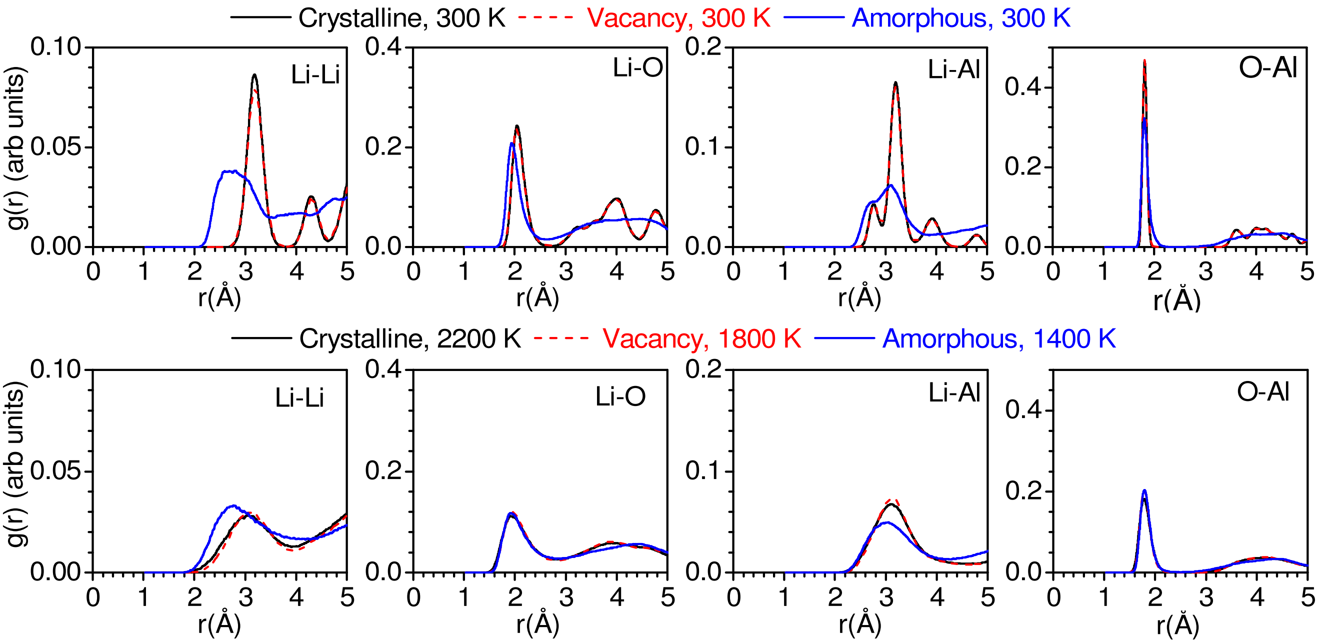

FIG. 4. The calculated pair distribution functions (PDFs) of various pairs of atoms in the crystalline phase, Li-vacancy structure, and amorphous LiAlO$_2$. The top and bottom panel corresponds to 300 K and high-temperature simulation, respectively.

located in a rather shallow and highly anharmonic potential. Therefore, with increasing temperature, the vibrational $\langle u^2 \rangle$ would increase significantly, and so would the Debye-Waller factor [$2W(Q) = Q^2\langle u^2 \rangle$]. Phonon anharmonicity is expected to lead to the large broadening and loss of peak structure in the Li partial DOS upon warming due to reduced phonon lifetimes. In addition, the increasingly large Debye-Waller factor suppresses the contribution of the Li DOS to the measured total DOS. These effects are most pronounced in the frequency range where Li has a significant contribution to the DOS. Thus, the observed effects in the measured DOS are attributable to the large anharmonicity and shallow nature of the Li potential, which reflects Li diffusion at high temperatures. The MSD as used to extract the diffusion coefficient is not restricted to the vibrational component but includes the jumps between equilibrium-metastable sites. The large vibrational $\langle u^2 \rangle$ of the Li atoms is visible in the trajectories shown in Sec. IV C 1. It is also important to note that the average residence time of Li at their equilibrium sites are much greater than the jump time (travel time between sites); hence, for a large extent of time, Li atoms remain at their site and vibrate with a large amplitude, which leads to the Li vibration spectra extended up to 80 meV even at elevated temperatures.

Further, the anharmonicity at high temperatures and lengthening of the Al-O bond results in softening and broadening of the stretching modes ~95 meV in the INS spectra. The low-energy Li modes are found to soften upon warming. Raman measurements [25] showed that the modes at 220 cm^{-1} (27.3 meV), 366 cm^{-1} (45.4 meV), and 400 cm^{-1} (49.6 meV) broaden on heating, and their intensity weakens dramatically. The broadening of peaks observed in our phonon spectra [Fig. 2(a)] is in qualitative agreement with observations from Raman measurements.

The calculated partial DOS in the vacancy structure shows similar temperature trends as that in the crystalline phase. Interestingly, the amorphous phase does not show any peak-like structure in the partial or total DOS even at 300 K. However, the spectral weight shifts toward lower energy at 1400 K, especially prominently in the Li partial DOS. The main observation from the INS spectra in γ-LiAlO$_2$ and AIMD simulations for all three phases of LiAlO$_2$ is the significant softening and broadening of Li vibrations, which mainly occur due to large MSD and Li diffusion at elevated temperatures.

B. Pair-distribution function

The environment surrounding lithium atoms is important to understand the pathways of Li diffusion in the material. The computed PDF for different atom pairs in crystalline γ-LiAlO$_2$ at 300 K are shown in Figs. 4 and S4 (Supplemental Material [55]). They show well-defined peaks corresponding to Li-Li, Li-O, Li-Al, and Al-O bond lengths in the crystalline phase. The first peak in $g(r)$ for Al-O arises from the bonds at 1.80 Å, while the peak corresponding to Li-O appears at 2.00 Å. The same behavior is also observed in the vacancy structure at 300 K with slightly reduced intensity of the Li-O PDF which is due to a smaller overall number of Li. The PDF of various atomic pairs in the amorphous phase at 300 K only shows clear peak features for the first and second neighbors. The first peak in the Al-O PDF is found to be very sharp, while peaks for longer bonds get significantly broader. This reflects the limited change in the shape of the AlO$_4$ polyhedron in the amorphization process. However, the orientational and translational ordering between polyhedral units is lost. Another polyhedral unit LiO$_4$ is relatively soft and more

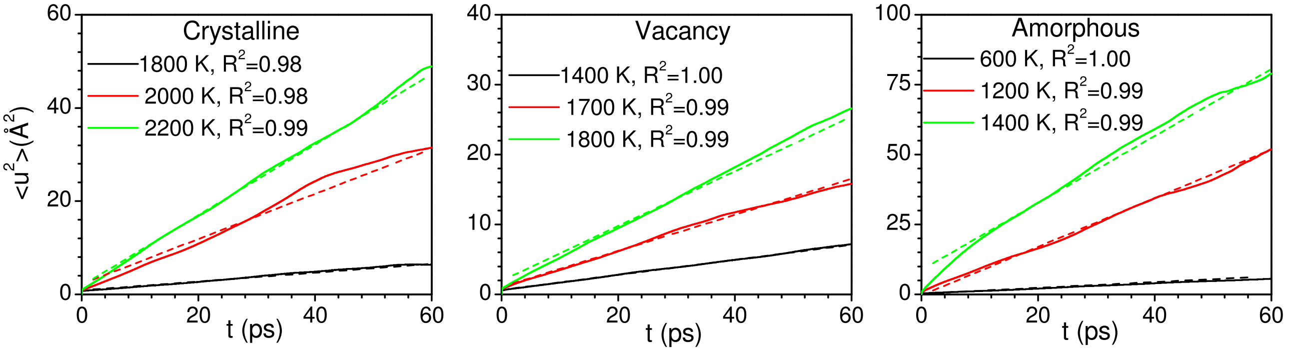

FIG. 5. Time-dependent mean-squared displacements (MSDs; $\langle u^2\rangle = \langle u_x^2\rangle + \langle u_y^2\rangle + \langle u_z^2\rangle$) of Li in γ-LiAlO$_2$, vacant LiAlO$_2$, and amorphous LiAlO$_2$ as obtained from *ab initio* molecular dynamics (AIMD) simulations at elevated temperatures. The estimated diffusion constant from linear fit is shown in Table II. The goodness of fit (R^2) for linear fit of each MSD plot is also shown. The MSD plots of Al and O are shown in Fig. S5, Supplemental Material [55]. The goodness of fit parameter (R) of linear fit of each MSD is also given.

strongly distorted during amorphization and therefore reveals a broad peak in the Li-O PDF. All other pairs of atoms also have significantly broader PDF features, which characterizes amorphization in simulation.

C. Lithium diffusion

In the γ-LiAlO$_2$, Li occupies the tetrahedral sites. The framework structure formed by AlO$_4$ units provides 3-*d* channels for Li transportation. However, the channel diameter is not homogenous and exhibits bottlenecks formed by polyhedral corner oxygen. Our AIMD simulations show that, in the ideal crystalline structure (γ-LiAlO$_2$) at 1800 K and above, Li diffusion occurs along these channels, but it is hindered due to strong repulsive interaction between O and Li at bottleneck points. The Li ions may pass through these strongly repulsive barriers either with sufficient kinetic energy (high temperature) or upon expanding the diameter of the bottleneck (by expanding the lattice or reorienting the polyhedral units). Interestingly, by amorphization, one can achieve randomly oriented polyhedral units as well as lower density of the material, which may facilitate the diffusion process. We simulated the amorphous structure through quenched annealing, as described above. The AIMD simulations of the crystalline and amorphous phases bring out the role of phonons and polyhedral reorientation on the diffusion behavior. In the following section, we will describe the mechanism of Li diffusion in all three configurations of LiAlO$_2$.

1. *Perfect crystalline* LiAlO$_2$

The calculated MSD of Li as a function of time in the perfect crystalline phase of LiAlO$_2$ at elevated temperatures are plotted in Figs. 5 and S5 (Supplemental Material [55]). We have also estimated the diffusion coefficient using a linear fit. Below 1600 K (Fig. S5, Supplemental Material [55]), the MSDs oscillate about their respective mean values and do not show any drift in time, corresponding to the regular behavior of a nondiffusing material. At temperatures above 1800 K, we observe a linear increase in time of Li MSD, while Al and O MSDs remain constant around their mean positions. This indicates the diffusion of Li within a stable host lattice. The host lattice stability at elevated temperatures is one of the important and desired properties of solid-state battery materials.

In Fig. 5, we have shown the MSD values averaged over all Li atoms. However, monitoring of the individual atomic trajectory and MSD provides insights into the diffusion behavior. Hence, in Fig. 6, we have also plotted the MSD of individual Li atoms. To explain the observed jump in individual Li MSD, we provide the Li-Li bond distances up to fifth neighbor in Table I. The first neighbor distance between Li-Li is ~3.18 Å, and a jump along this bond contributes a step increase in MSD ~10.1 Å^2 (Li has four first neighbors in LiAlO$_2$). It can be observed from Fig. 6 that most of the MSD

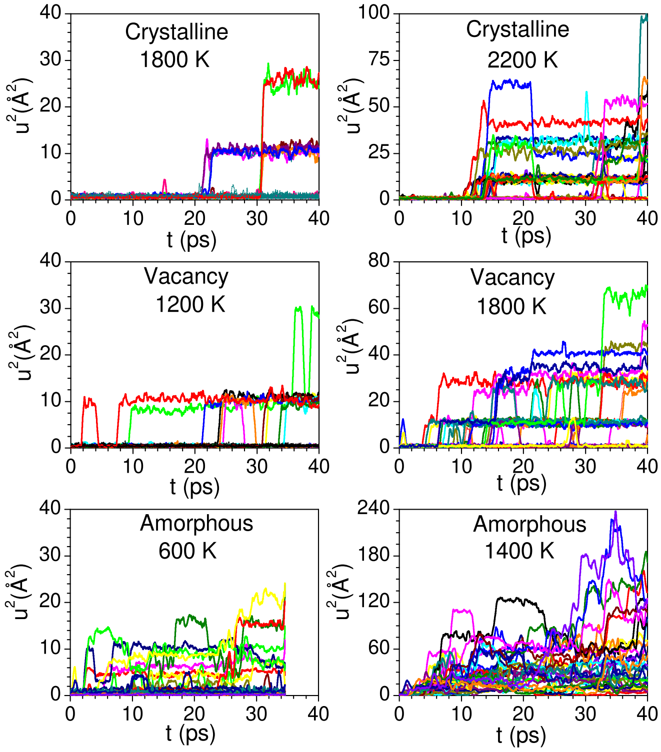

FIG. 6. The *ab initio* molecular dynamics (AIMD) calculated squared displacement (u^2) of individual Li atoms as a function of time in the perfect crystalline phase, vacancy structure, and amorphous phase of LiAlO$_2$ at different temperatures (indicated in each panel). The plots of various lithium atoms are shown by different colors to distinguish the jumps of different atoms.

TABLE I. Calculated Li-Li distance vectors and the distances in γ-LiAlO$_2$ at 300 K up to fifth nearest neighbors. The unit cell has four Li atoms at Li0 (0.68613, 0.31387, 0.25), Li1(0.18613, 0.18613, 0.5), Li2 (0.31387, 0.68613, 0.75), and Li3 (0.81387, 0.81387, 0). The unit cell parameters as used in *ab initio* calculations are $a = b = 5.3302$ Å, $c = 6.4016$ Å; ΔX, ΔY, and ΔZ are the difference in the X, Y, and Z coordinates between two lithium atoms; d is the interatomic distance between two lithium atoms.

	ΔX fractional	ΔY fractional	ΔZ fractional	ΔX (Å)	ΔY (Å)	ΔZ (Å)	ΔX^2 (Å^2)	ΔY^2 (Å^2)	ΔZ^2 (Å^2)	d (Å)	d^2 (Å^2)
Li1-Li0	−0.5	−0.1277	0.25	−2.67	−0.68	1.60	7.12	0.46	2.56	3.18	10.11
Li2-Li0	−0.3723	0.3723	0.5	−1.98	1.98	3.2	3.92	3.92	10.24	4.26	18.15
Li3-Li1	0.6277	0.3723	−0.5	3.35	1.98	−3.2	11.22	3.92	10.24	5.04	25.40
Li0-Li0	0	1	0	0	5.33	0	0	28.4	0	5.33	28.41
Li0-Li0	0	0	1.0	0	0	6.40	0	0	40.98	6.40	40.96

steps in crystalline and vacancy LiAlO$_2$ at 800 and 2200 K are dominated by first neighbor jumps. The second neighbor distance of Li-Li is ~4.26 Å (MSD ~18 Å^2); it is interesting to note that we do not observe any direct second neighbor Li-Li jump. Hence, these observations clearly suggest that the barrier energy along pathways connecting the first neighbors is smaller and different from second neighbor pathways. The absence of a second neighbor jump is due to much closer distances between Li and O along the pathways. In Fig. 6, we also observe a higher jump in MSD values ~25 Å^2, which corresponds to the third neighbor Li-Li pairs. We also notice from Fig. 6 that, in the crystalline structure at 1800 K, simultaneous jumps occur for several atoms, revealing a correlated jump behavior. Isolated jumps between nearest neighbor sites in the perfect crystalline structure are not probable since there are no vacant sites. However, as we will discuss below, such independent jumps do occur in the vacancy structure and the amorphous structure. As the temperature is increased to 2200 K, Li atoms show (Fig. 6) large displacements in the AIMD simulations. These MSDs match very well with the calculated jump displacements of lithium atoms between the third, fourth, and fifth neighbor sites (Table I) of 25.40, 28.41, and 40.96 Å^2, respectively, which confirms that the diffusion process is governed by the jump diffusion model [64,65].

The AIMD calculated trajectories of selected Li atoms in the crystalline phase of γ-LiAlO$_2$ are shown in Fig. 7, which confirms that, at 1800 K, there are jumps of Li atoms from one tetrahedral site to another. As the temperature is increased to 2200 K, the diffusion of Li is also through longer jumps; however, we also find an increase in the number of Li jumps from one tetrahedral site to another site. Large amplitude librations and reorientations of AlO$_4$ polyhedra help the Li diffusion process, as we will discuss later.

2. *Vacancy in crystalline* LiAlO$_2$

Vacancies and defects are known to enhance diffusion [66–68]. Usually, in solid ionic conductors, the diffusing ions hop from one occupied site to another unoccupied site. The unoccupied sites could be interstitial or atomic sites. In the absence of unoccupied sites in crystals, the ions can diffuse by simultaneous jumps of two or more ions, leading to a cooperative or correlated diffusion. Also, in the case of the perfectly crystalline phase, the Li diffusion is limited since it has to overcome the interaction energy of nearby host elements as well as from Coulomb interaction with the nearby occupied Li sites. Fully occupied sites along the diffusion path preclude adjusting or reorganizing the host framework to create enough room for Li migration. However, the presence of vacancies usually enhances the diffusion behavior by relaxing these constraints. We investigated the effect of Li vacancies in LiAlO$_2$, with one Li vacancy among 32 Li sites in the $2 \times 2 \times 2$ supercell of crystalline γ-LiAlO$_2$. The calculated MSD of each species in the vacancy structure from 300 to 1800 K is shown in Figs. 5 and S5 (Supplemental Material [55]). We did not observe Li diffusion <1200 K within a simulation time ~20 ps. At 1200 K, Li ions start diffusing in the system, while the Al and Si form a stable framework. By following individual Li trajectories, we found a jump in MSD values of ~10.1 Å^2, which corresponds to the minimum Li-Li distance in LiAlO$_2$. At still higher temperatures (1800 K and above), many such jumps are observed, with jump lengths like those in the perfect crystalline structure. However, fewer simultaneous jumps occur than in the crystalline structure. The MSD slope at 1800 K (Fig. 5) is about four times larger in the vacant LiAlO$_2$ than in the perfect crystalline structure, which also reflects in the respective diffusion constant. The displacements of Li atoms, as shown in Fig. 6, show that magnitude of displacements is nearly the same as that in the crystalline phase; however, in the vacancy structure, we find that more Li atoms are diffusing than the perfect crystalline structure.

Our AIMD simulations show a significant enhancement in diffusion from the presence of Li vacancies in crystalline LiAlO$_2$. We observed similar pathways for jump diffusion in both cases. It seems that one can achieve the Li diffusion in the presence of vacancy in systems where the presence of vacant sites helps to reduce the dependence on the polyhedral dynamics necessary for the Li diffusion process in the stoichiometric compound. The calculated trajectories of selected Li atoms in the vacancy structure (Fig. 7) at 1200 and 1800 K confirm that vacancy leads to enhancement of the Li diffusion process in comparison with that in the crystalline phase. However, the diffusion process in both structures occurs only through discrete Li jumps from one tetrahedral site to another.

Due to the relatively weaker bonding of Li with the host, the Li vacancies are more likely than that of oxygen. At high temperatures, the compound could also exhibit oxygen vacancies. We have performed additional calculations (Fig. S6, Supplemental Material [55]) with two lithium and one oxygen vacancy. Even with the oxygen vacancies, we do not find any oxygen diffusion at temperatures up to 1800 K, while we observe Li diffusion.

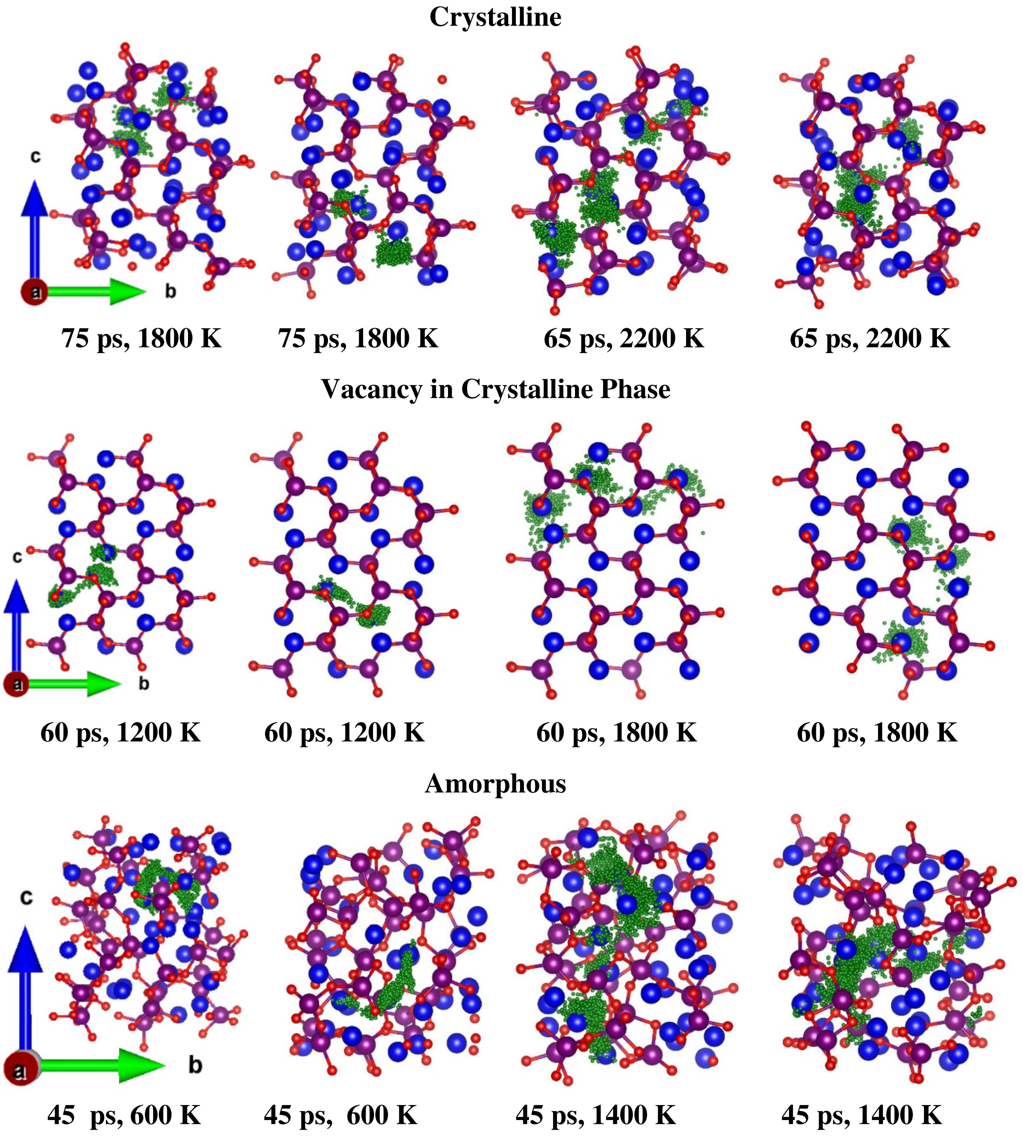

FIG. 7. Computed trajectories of selected Li atoms in the perfect crystalline phase, vacancy structure, and amorphous phase of $LiAlO_2$. Red, blue, and violet spheres represent oxygen, lithium, and aluminium atoms, respectively, at their lattice sites. The time-dependent positions of the selected lithium atoms are shown by green dots. The numbers below each frame indicate the duration of trajectory of Li and temperature of the simulation. Each figure shows the full simulation cell ($2 \times 2 \times 2$ cell of γ-$LiAlO_2$).

3. Amorphous $LiAlO_2$

The introduction of disorder in γ-$LiAlO_2$ is known to increase [24,37] the Li ion conduction. The polyhedral orientational disorder in the amorphous structure is also known to enhance [38,69–71] the diffusion behavior in other compounds. Many graphite/carbon-based materials [72–74] are known to exhibit enhanced diffusion in the amorphous form compared with their crystalline phases. Our AIMD simulation in the amorphous phase of $LiAlO_2$, strikingly, shows Li diffusion occurring at 600 K, which is (Figs. 4 and S5, Supplemental Material [55]) much lower than in crystalline and vacant phases. The PDF of the amorphous phase at 300 K (Figs. 4 and S4, Supplemental Material [55]) shows that only the first neighbor Al-O and O-O peaks are well defined, with a broad distribution at larger bond lengths suggesting orientationally disordered polyhedral units. Interestingly, the Li-Li PDF shows a broad distribution even around the first neighbor distance at 3.0 Å (Fig. 4). These first neighbor Li-Li correlations are stabilized due to misoriented AlO_4 polyhedral units. Further, the amorphous phase exhibits significantly smaller first neighbor Li-Li distances, which may enhance the Li hoping probability. The Al-O PDF does not show the pronounced temperature change seen in the Li-Li PDF. We also notice that the peaks in Li-O and O-O do show significant changes with temperature, which is due to the fact that, at high temperatures, the randomly oriented AlO_4 polyhedra are kinetically activated. Unlike in the crystalline phase, the diffusion in the amorphous phase appears (Fig. 6) to be like that of a liquid. The calculated trajectories of some of the Li atoms (Fig. 7) at 600 and 1400 K confirm a broad distribution of Li displacements in the diffusion process. It appears that due to the misorientation of AlO_4 polyhedra and the more

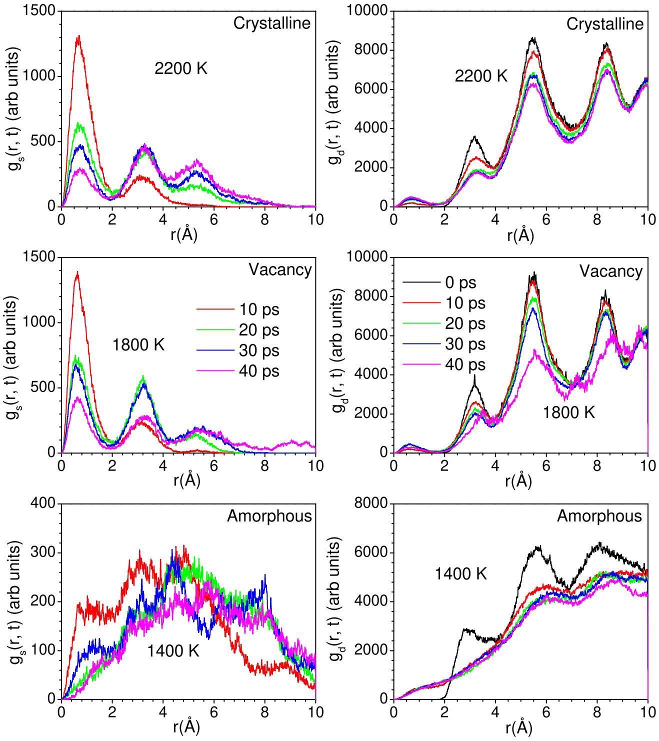

FIG. 8. The self [$g_s(r,t)$] and distinct [$g_d(r,t)$] Van Hove correlation functions in LiAlO$_2$, computed based on *ab initio* molecular dynamics (AIMD), for the perfect crystalline phase, vacancy structure, and the amorphous phase.

distributed Li-Li bond distances, new low energy pathways for Li diffusion are available in the amorphous structure as compared with those available in the crystalline and vacant structure.

D. Van Hove pair correlation function

To further investigate the time evolution of the diffusion process, we have computed the Van Hove self $g_s(r,t)$ and distinct $g_d(r,t)$ correlation functions [59] between Li atoms. We show g_s and g_d in Fig. 8, left and right panels, respectively, at different time intervals. The calculations shown at elevated temperatures correspond to Li diffusion occurring in all three phases. At $t = 0$, g_s is a δ function at $r = 0$; hence, it is not shown. At later times, the first peak in g_s at $\sim$1 Å corresponds to Li vibrational amplitude, and the height of this peak decreases with time, inferring that few of the Li ions diffuse, thus limiting the magnitude of g_s at farther distances. In the crystalline phase, at 10 ps, a peak develops in g_s at $\sim$3 Å and grows in intensity with time. From 10 ps onward, we see that another peak appears at $\sim$5 Å. These peak positions correspond to the distances between neighboring Li sites in the crystal structure, thus suggesting that the Li ions diffuse via discrete jumps. Similarly, in the vacancy configuration, we also see peaks at the same distances of $\sim$3 and 5 Å, but the diffusion process is faster. On the other hand, in the amorphous phase, $g_s(r,t)$ does not exhibit any sharp peaks but rather a broad feature, which reflects that the diffusive process in this phase is not restricted to jumps between periodic sites. This indicates a more homogeneous spatial environment than in the crystalline phases. This homogeneity in space is attributed to randomly oriented polyhedral units resulting in local metastable diffusion paths.

In Fig. 8 (right panels), we show the Li-Li distinct Van Hove correlation function g_d, which gives the probability of finding two distinct Li atoms separated by distance r and time t. In other words, given a Li atom at $r = 0$ and $t = 0$, this shows how the distance-distribution of other Li atoms evolves with time t. We observe sharp peaks at $t \to 0$ due to the crystalline structure, which correspond to various Li-Li bond distances in the static structure. The diffusion process leads to a reduced probability of finding two Li at the static bond distances; however, the lost intensity is observed in between these distances. When a random diffusion process occurs, the peak intensity continually decreases. However, when two Li are diffusing in a correlated manner, the intensity of the peak corresponding to interatomic distances will slightly reduce, but the peak structure will remain over a long period of time. In the case of crystalline LiAlO$_2$, we observe that the first neighbor peak intensity does not significant decay with time, indicating the short-range correlation behavior. The jump diffusion in the perfect crystalline structure occurs between lattice sites without any interstitial site. This necessitates correlated diffusion as there are no vacant sites available. The vacant crystalline phase shows a mix of correlated and uncorrelated jump diffusion. The amorphous phase exhibits both jump and continuous diffusion but not correlated jump behavior.

E. Polyhedral reorientation and lithium diffusion

Interestingly, in the crystalline phase, all the observed MSD jumps correspond to the Li-Li neighbor distance. Hence, this infers a negligible probability for the presence of the Li interstitial site in the crystalline as well as in vacant LiAlO$_2$. Thus, without vacancy or interstitial sites, another mechanism must enable Li diffusion. This can be better understood by monitoring the Al-O bond angle projection to the z and x axes. In Figs. 9 and S10 (Supplemental Material [55]), we plotted the bond angle projections of a few selected polyhedra as a function of time at different temperatures in the crystalline phase. We find that, at 300 K, the angles are fluctuating within a few degrees, which is common in stable crystalline materials. However, at 2200 K, the angles show large fluctuation and even polyhedral reorientation. The large vibrational amplitude of AlO$_4$ units widens the Li hopping channel and significantly reduces the barrier energy for Li hopping between two Li tetrahedral sites. Hence, this shows that the Li diffusion is correlated with larger vibrational amplitude of these polyhedral units. The correlation factor also depends on the volume of the material or density. Materials with a high volume per atom may not show such correlations since the wider diffusion channels are not affected as much by framework polyhedra dynamics. To show the correlation between polyhedral reorientational dynamics and Li diffusion, we have shown the time dependence of bond angles of a few selected AlO$_4$ units and nearest Li MSD in Fig. 9. The nearly simultaneous jump in bond angle and MSD of nearest Li indicates the strong correlation between the polyhedral dynamics and Li diffusion.

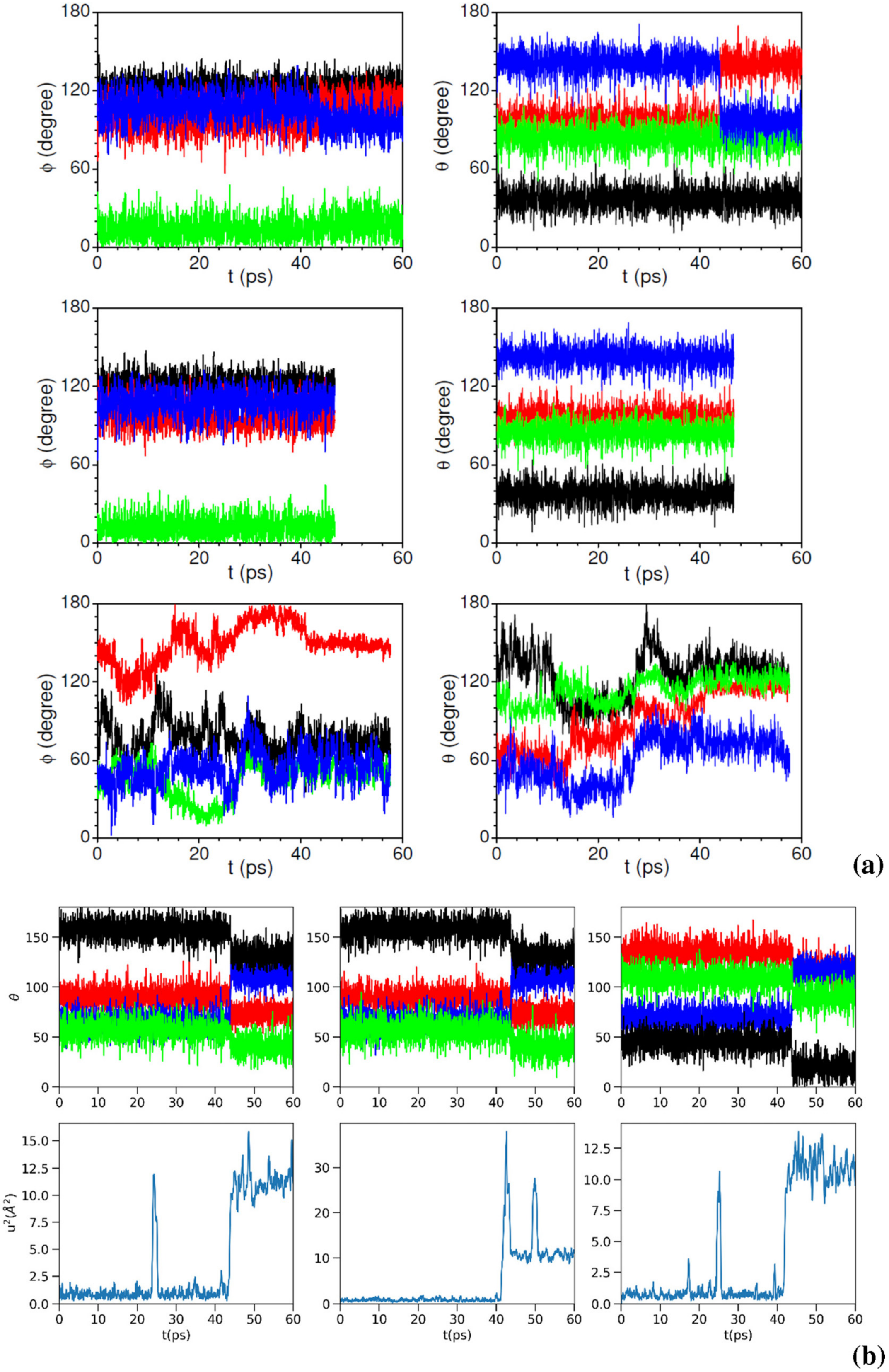

FIG. 9. (a) (top) The computed angle between various Al-O bonds and crystallographic z axis (θ) and x axis (φ) for a representative AlO_4 polyhedral unit at elevated temperatures in $LiAlO_2$ for the perfect crystalline phase, vacancy structure, and the amorphous phase. (b) (bottom) The calculated time dependence of bond angles of Al-O in selected polyhedral units and mean-squared displacement (MSD) of nearest Li atom in the crystalline $LiAlO_2$ at 2200 K.

TABLE II. The estimated diffusion coefficient from MSD and VACF. The estimated RSD of the diffusion coefficient (D) as described in Ref. [62]. The analysis was performed on 80 ps (marked with *) and 60 ps (marked with †) trajectory length.

Phase	T (K)	D(10^{-10} m^2/s) estimated from VACF/MSD	Max MSD (Å^2)	TMSD (Å^2) max MSD*N$_{\text{Li}}$	$N_{\text{eff}} = \text{TMSD}/(d_{\text{jump}}{}^2)$ $d^2{}_{\text{jump}} \sim 10$	RSD of D $3.43/\sqrt{N_{\text{eff}}} + 0.04$
CRYSTAL*	2200	10.6/12.6	51	1632	163	0.31
CRYSTAL*	2000	9.2/8.1	37	1184	118	0.36
CRYSTAL*	1800	1.6/1.6	7	224	22.0	0.77
AMORPHOUS*	1400	21.7/20.0	90	2880	288	0.24
AMORPHOUS†	1200	19/14.5	61	1952	195	0.29
AMORPHOUS†	1000	9.5/10.7	20	640	64	0.47
AMORPHOUS†	800	4.13/4.4	12	384	38	0.60
AMORPHOUS*	600	1.6/1.7	6	192	19	0.82
VACANCY*	1800	7.0/6.5	34	1054	105	0.37
VACANCY*	1700	4.0/4.3	22	682	68	0.46
VACANCY*	1600	2.6/2.2	16	496	50	0.52
VACANCY*	1400	1.0/1.8	9	279	28	0.69

In the case of LiAlO$_2$ with vacancies, we also observe large fluctuations in AlO$_4$ bond angles. Thus, vacancies and polyhedral dynamics both contribute to enhancing the diffusion of Li. Interestingly, in the amorphous phase, we do find that bond angles show a large vibrational amplitude along with a shift of their mean values. Hence, the metastable frozen AlO$_4$ units in the amorphous phase start reorienting at elevated temperature, which also drags or helps Li to migrate from one site to another and enhances the Li diffusion.

We analyzed the distribution of several bond angles, specifically O-Al-O and Al-O-Al. These angles at 300 K are plotted in Fig. S9 (Supplemental Material [55]). The O-Al-O bond angle is related to the geometry and rigidity of the AlO$_4$ polyhedral units. We can see that, in both the perfect crystalline structure and the vacancy structure, the geometry of the AlO$_4$ tetrahedra is very well maintained since the average bond angle O-Al-O is close to 109°. In the amorphous phase also, we see that the bond angle distribution peaks ∼109°, but with a significant spread compared with the crystalline structure, indicating some level of distortion of the tetrahedra. The Al-O-Al bond angle, corresponding to the angle between two corner-sharing tetrahedra, shows a broad distribution in the amorphous phase, which indicates that the tetrahedra are somewhat randomly oriented.

F. Diffusion coefficient

We have computed the diffusion coefficient in all three phases at elevated temperatures. At low temperatures, the Li diffusion is very small and needs a very large trajectory (in nanoseconds) to observe the significant Li diffusion event, which is difficult to achieve with AIMD methods. While at elevated temperatures, the Li diffusive events become more pronounced, and an ∼80 ps trajectory would be sufficient to estimate the diffusion coefficient. We determined the Li diffusion constant from the Li MSD slope as well as by integrating the VACF [75] of Li. The calculated diffusion coefficients from both methods are listed in Table II. Both methods give very similar values of the diffusion coefficient, justifying the sufficient sampling of the diffusive regime. Further, we have calculated the relative standard deviation (RSD) of the estimated diffusion constant (Table II) using an empirical relation as described in Ref. [62]. The RSD of the diffusion constant depends on the number of total jump events during the simulation time (N_{eff}) as given by

$$\text{RSD} = 3.43/\sqrt{N_{\text{eff}}} + 0.04, \tag{5}$$

$$N_{\text{eff}} = \text{TMSD}/d_{\text{jump}}{}^2, \tag{6}$$

where TMSD is the total MSD defined as the sum of all Li MSDs in the simulation cell, and d_{jump} is the mean jump length of the Li atom. In the case of crystalline and vacant LiAlO$_2$, the mean jump length is ∼3.18 Å. In the case of amorphous LiAlO$_2$, there is a distribution of jump length, and it is difficult to define an effective jump length; hence, for the sake of comparison, we considered the same d_{jump} used in crystalline and Li-vacant LiAlO$_2$.

The linear fit of the slope of the Li MSD with time at different temperatures and estimated diffusion coefficients [60] are shown in Fig. 10. To estimate the activation energy, the temperature dependence of the diffusion coefficient is fitted with an Arrhenius relation (Fig. 10), i.e.,

$$D(T) = D_0\exp(-E_a/k_BT), \tag{7}$$

or equivalently,

$$\ln[D(T)] = \ln(D_0) - E_a/k_BT, \tag{8}$$

where D_0 is a constant factor representing the diffusion coefficient at infinite temperature, E_a is the activation energy, k_B is the Boltzmann constant, and T is temperature in Kelvin. We find that the self-diffusion coefficient of Li ions exceeds 10^{-10} m^2/s in the crystalline phase, vacancy structure, and amorphous structure at 1800, 1200, and 600 K, respectively. One may notice that the plot of ln(D) vs 1000/T [Figs. 10(a)–10(c)] does not appear to strictly follow the

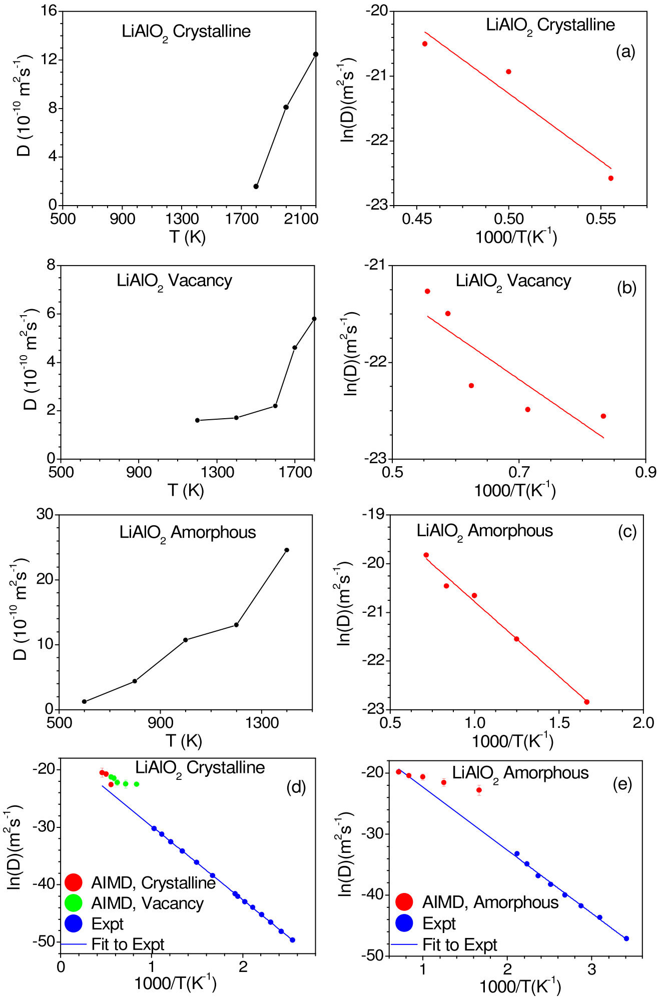

FIG. 10. The calculated diffusion coefficients and activation energy barriers in the (a) perfect crystalline phase, (b) vacancy structure, and (c) amorphous phase of LiAlO$_2$ using *ab initio* molecular dynamics (AIMD) simulations. (d) and (e) The comparsion between the experimental and calculated diffusion coefficient. The experimental data of diffusion coefficient in crystalline phase are available only up to 1000 K [21], while in the amorphous phase, Li diffusion coefficient data [37] are available up to 473 K. We have extrapolated the experimental data (considering the Arrhenius behavior) at high temperatures and compared with our AIMD estimated diffusion constants.

Arrhenius behavior, which could be due to the limited length of AIMD trajectories.

The available experimental data of diffusion coefficients in crystalline [21] and amorphous phases [37] were measured up to 1000 and 473 K, respectively, and their values are $<10^{-12}$ m^2/s. To sense this small value using AIMD requires a very large trajectory (in nanoseconds), which is not practical within the AIMD framework. However, in the higher temperature regime, where the diffusion coefficients approach $\sim10^{-10}$ m^2/s, it can be well captured with AIMD simulation within a few tens of picoseconds. Therefore, we have extrapolated the experimental data (considering the Arrhenius behavior) at high temperatures and compared them with our AIMD estimated diffusion constants [Figs. 10(d) and 10(e)], which show a fair comparison between the simulations and the extrapolated experimental values. We may note that, within the limitations of the AIMD simulations, especially the small cell and time, we cannot expect to determine precise values of the diffusion coefficient and the activation energy, but we can indeed describe the underlying physics governing the diffusion processes.

Despite the practical limitations of the AIMD simulations, it may be of interest to compare the values of the activation energy of Li diffusion with reported experimental values. As the previous study [21] observed, a significant difference exists in the activation energy in powder and single-crystal LiAlO$_2$ due to different concentrations of impurities and defects in these samples. Our simulation was performed in an ideal crystalline phase without extrinsic or intrinsic defect. The experimentally reported value is 1.14 eV [26] from single-crystal experiments, while the values from other powder and single-crystal experiments are in the range of 0.7–1.5 eV [21]. The activation energy from simulations in the perfect crystalline phase is found [Fig. 10(a)] to be 1.8(5) eV. In the case of the vacancy structure, we find [Fig. 10(b)] the activation energy of 0.4(2) eV. This small value is perhaps due to a large vacancy concentration ($\sim$3%) in the simulation. The range of these simulated values for the perfect crystalline structure and the large vacancy structure are in good qualitative agreement with the range of experimental values. We note that there is a perceptible decrease in the simulated value of the activation energy from the perfect crystal structure to the vacancy structure, suggesting that the presence of vacancies could significantly lower the barrier. In the amorphous phase, we find the activation energy to be 0.26(2) eV [Fig. 10(c)], which is much lower than the experimentally reported value of 0.9 eV [37]. The lowering of the activation energy in the amorphous structure compared with the crystalline structure agrees with the experimental observations, showing that disorder facilitates [24,37] Li diffusion. Further, an important result is that the diffusion occurs in the amorphous structure at a much lower temperature than that in the crystalline structure. The emergence of shorter pathways along with comparatively lower barrier energies attributed to misorientation and distortion of the polyhedral units in the amorphous phase led to the Li diffusion at lower temperatures.

V. CONCLUSIONS

Our AIMD simulations, combined with INS measurements, enabled us to rationalize the diffusion mechanism in LiAlO$_2$. We can understand Li diffusion in γ-LiAlO$_2$ in terms of well-defined jumps between lattice sites in the crystal, while a combination of jumplike and continuous diffusion occurs in the amorphous phase. The activation energy for the diffusion processes was obtained in various phases. The presence of Li vacancies and disorder in the amorphous structure significantly reduces the Li diffusion onset temperature in comparison with the ideal crystalline phase. The lower onset temperature in the amorphous phase, along with lower activation energy and larger diffusion coefficient, occurs due to the availability of additional diffusion pathways around favorably oriented AlO$_4$ polyhedra as compared with those in the crystalline structure. We showed that more flexible polyhedral units are likely to enhance the Li diffusion in these systems. By amorphizing the structure, we provide more room for polyhedral dynamics/flexibility besides creating more metastable Li sites, which easily percolates the Li diffusion process. Our temperature-dependent INS measurements and AIMD simulations also show that the Li diffusion is reflected in the significant broadening of the phonon spectrum. This paper suggests that designing materials with a flexible polyhedral framework structure will likely give large ionic conductivity. Further, by amorphization and optimizing the Li-vacancy concentration, one can tune the operating temperature of Li diffusion.

ACKNOWLEDGMENTS

The use of ANUPAM supercomputing facility at BARC is acknowledged. S.L.C. acknowledges the financial support of the Indian National Science Academy for INSA Senior Scientist position. O.D. acknowledges financial support from Duke University through startup funds.

[1] H. Li, Joule **3**, 911 (2019).

[2] S. Randau, D. A. Weber, O. Kötz, R. Koerver, P. Braun, A. Weber, E. Ivers-Tiffée, T. Adermann, J. Kulisch, and W. G. Zeier, Nat. Energy **5**, 259 (2020).

[3] Y. Shen, Y. Zhang, S. Han, J. Wang, Z. Peng, and L. Chen, Joule **2**, 1674 (2018).

[4] J. Liu, Z. Bao, Y. Cui, E. J. Dufek, J. B. Goodenough, P. Khalifah, Q. Li, B. Y. Liaw, P. Liu, and A. Manthiram, Nat. Energy **4**, 180 (2019).

[5] Z. Gao, H. Sun, L. Fu, F. Ye, Y. Zhang, W. Luo, and Y. Huang, Adv. Mater. **30**, 1705702 (2018).

[6] K. Takada, J. Power Sources **394**, 74 (2018).

[7] J. Motavalli, Nature **526**, S96 (2015).

[8] S. Ohno, A. Banik, G. F. Dewald, M. A. Kraft, T. Krauskopf, N. Minafra, P. Till, M. Weiss, and W. G. Zeier, Prog. Energy **2**, 022001 (2020).

[9] R. Xu, F. Han, X. Ji, X. Fan, J. Tu, and C. Wang, Nano Energy **53**, 958 (2018).

[10] A. Manthiram, X. Yu, and S. Wang, Nat. Rev. Mater. **2**, 1 (2017).

[11] Y. Xiao, Y. Wang, S.-H. Bo, J. C. Kim, L. J. Miara, and G. Ceder, Nat. Rev. Mater. **5**, 105 (2020).

[12] A. Banerjee, X. Wang, C. Fang, E. A. Wu, and Y. S. Meng, Chem. Rev. **120**, 6878 (2020).

[13] S. Wenzel, S. Randau, T. Leichtweiß, D. A. Weber, J. Sann, W. G. Zeier, and J. R. Janek, Chem. Mater. **28**, 2400 (2016).

[14] L. Porz, T. Swamy, B. W. Sheldon, D. Rettenwander, T. Frömling, H. L. Thaman, S. Berendts, R. Uecker, W. C. Carter, and Y. M. Chiang, Adv. Energy Mater. **7**, 1701003 (2017).

[15] Y. Ren, Y. Shen, Y. Lin, and C.-W. Nan, Electrochem. Commun. **57**, 27 (2015).

[16] F. Han, J. Yue, X. Zhu, and C. Wang, Adv. Energy Mater. **8**, 1703644 (2018).

[17] W. D. Richards, L. J. Miara, Y. Wang, J. C. Kim, and G. Ceder, Chem. Mater. **28**, 266 (2016).

[18] J. M. Whiteley, J. H. Woo, E. Hu, K.-W. Nam, and S.-H. Lee, J. Electrochem. Soc. **161**, A1812 (2014).

[19] M. M. Islam, J. Uhlendorf, E. Witt, H. Schmidt, P. Heitjans, and T. Bredow, J. Phys. Chem. C **121**, 27788 (2017).

[20] D. Wiedemann, S. Indris, M. Meven, B. Pedersen, H. Boysen, R. Uecker, P. Heitjans, and M. Lerch, Z. Kristallogr. Cryst. Mater. **231**, 189 (2016).

[21] D. Wiedemann, S. Nakhal, J. Rahn, E. Witt, M. M. Islam, S. Zander, P. Heitjans, H. Schmidt, T. Bredow, M. Wilkening, and M. Lerch, Chem. Mater. **28**, 915 (2016).

[22] E. Witt, S. Nakhal, C. V. Chandran, M. Lerch, and P. Heitjans, Z. Phys. Chem. **229**, 1327 (2015).

[23] M. M. Islam and T. Bredow, J. Phys. Chem. Lett. **6**, 4622 (2015).

[24] D. Wohlmuth, V. Epp, P. Bottke, I. Hanzu, B. Bitschnau, I. Letofsky-Papst, M. Kriechbaum, H. Amenitsch, F. Hofer, and M. Wilkening, J. Mater. Chem. A **2**, 20295 (2014).

[25] Q. Hu, L. Lei, X. Jiang, Z. C. Feng, M. Tang, and D. He, Solid State Sci. **37**, 103 (2014).

[26] S. Indris, P. Heitjans, R. Uecker, and B. Roling, J. Phys. Chem. C **116**, 14243 (2012).

[27] S. J. Heo, R. Batra, R. Ramprasad, and P. Singh, J. Phys. Chem. C **122**, 28797 (2018).

[28] P. Waltereit, O. Brandt, A. Trampert, H. T. Grahn, J. Menniger, M. Ramsteiner, M. Reiche, and K. H. Ploog, Nature **406**, 865 (2000).

[29] J. Charpin, F. Botter, M. Briec, B. Rasneur, E. Roth, N. Roux, and J. Sannier, Fusion Eng. Des. **8**, 407 (1989).

[30] F. Botter, F. Lefevre, B. Rasneur, M. Trotabas, and E. Roth, J. Nucl. Mater. **141**, 364 (1986).

[31] J.-P. Jacobs, M. A. San Miguel, L. J. Alvarez, and P. B. Giral, J. Nucl. Mater. **232**, 131 (1996).

[32] H. Tsuchihira, T. Oda, and S. Tanaka, J. Nucl. Mater. **414**, 44 (2011).

[33] M. Marezio, Acta Crystallogr. **19**, 396 (1965).

[34] X. Li, T. Kobayashi, F. Zhang, K. Kimoto, and T. Sekine, J. Solid State Chem. **177**, 1939 (2004).

[35] L. Lei, D. He, Y. Zou, W. Zhang, Z. Wang, M. Jiang, and M. Du, J. Solid State Chem. **181**, 1810 (2008).

[36] Y. Ikeda, H. Ito, G. Matsumoto, and H. Hayashi, J. Nucl. Sci. Technol. **17**, 650 (1980).

[37] J. Rahn, E. Witt, P. Heitjans, and H. Schmidt, Z. Phys. Chem. **229**, 1341 (2015).

[38] J. Cuan, Y. Zhou, T. Zhou, S. Ling, K. Rui, Z. Guo, H. Liu, and X. Yu, Adv. Mater. **31**, 1803533 (2019).

[39] B. Singh, M. Gupta, R. Mittal, and S. Chaplot, PCCP **20**, 12248 (2018).

[40] M. K. Gupta, B. Singh, P. Goel, R. Mittal, S. Rols, and S. L. Chaplot, Phys. Rev. B **99**, 224304 (2019).

[41] B. Singh, M. K. Gupta, R. Mittal, M. Zbiri, S. Rols, S. J. Patwe, S. N. Achary, H. Schober, A. K. Tyagi, and S. L. Chaplot, PCCP **19**, 15512 (2017).

[42] B. Singh, M. K. Gupta, R. Mittal, and S. L. Chaplot, J. Mater. Chem. A **6**, 5052 (2018).

[43] B. Singh, M. K. Gupta, R. Mittal, M. Zbiri, S. Rols, S. J. Patwe, S. N. Achary, H. Schober, A. K. Tyagi, and S. L. Chaplot, J. Appl. Phys. **121**, 085106 (2017).

[44] M. K. Gupta, S. K. Mishra, R. Mittal, B. Singh, P. Goel, S. Mukhopadhyay, R. Shukla, S. N. Achary, A. K. Tyagi, and

S. L. Chaplot, Phys. Rev. Mater. **4**, 045802 (2020).
[45] K. Sköld and D. L. Price, *Neutron scattering* (Academic Press, Orlando, 1986), Vol. A.
[46] J. M. Carpenter and D. L. Price, Phys. Rev. Lett. **54**, 441 (1985).
[47] S. Rols, H. Jobic, and H. Schober, C. R. Phys. **8**, 777 (2007).
[48] V. F. Sears, Neutron News **3**, 26 (1992).
[49] G. Kresse and J. Furthmüller, Comput. Mater. Sci. **6**, 15 (1996).
[50] G. Kresse and J. Furthmüller, Phys. Rev. B **54**, 11169 (1996).
[51] G. Kresse and D. Joubert, Phys. Rev. B **59**, 1758 (1999).
[52] J. P. Perdew, K. Burke, and M. Ernzerhof, Phys. Rev. Lett. **78**, 1396(E) (1997).
[53] J. P. Perdew, K. Burke, and M. Ernzerhof, Phys. Rev. Lett. **77**, 3865 (1996).
[54] S. Nosé, J. Chem. Phys. **81**, 511 (1984).
[55] See Supplemental Material at http://link.aps.org/supplemental/10.1103/PhysRevB.103.174109 for details about the calculated and experimental phonon spectra from MD and lattice dynamics calculations are given. It also includes the results of calculated PDFs, time-dependent MSDs, distribution of the bond angles and angle between various Al-O bonds and crystallographic z axis (θ) and x axis (φ) for a representative AlO_4 polyhedral unit.
[56] B. Cockayne and B. Lent, J. Cryst. Growth **54**, 546 (1981).
[57] M. P. Allen and D. J. Tildesley, *Computer Simulation of Liquids* (Oxford University Press, Oxford, 2017).
[58] V. Calandrini, E. Pellegrini, P. Calligari, K. Hinsen, and G. R. Kneller, Éc. Thémat. Soc. Fr. Neutron. **12**, 201 (2011).
[59] L. Van Hove, Phys. Rev. **95**, 1374 (1954).
[60] A. Einstein, Ann. Phys. Lpz **322**, 549 (1905).
[61] A. K. Sagotra, D. Chu, and C. Cazorla, Phys. Rev. Mater. **3**, 035405 (2019).
[62] X. He, Y. Zhu, A. Epstein, and Y. Mo, Npj Comput. Mater. **4**, 1 (2018).
[63] J. E. Turney, E. S. Landry, A. J. H. McGaughey, and C. H. Amon, Phys. Rev. B **79**, 064301 (2009).
[64] M. Bee, *Quasielastic Neutron Scattering: Principles and Applications in Solid-State Chemistry, Biology, and Materials Science* (IOP Publishing Ltd, Bristol, 1988).
[65] P. L. Hall and D. Ross, Mol. Phys. **42**, 673 (1981).
[66] J. Sugiyama, K. Mukai, Y. Ikedo, H. Nozaki, M. Månsson, and I. Watanabe, Phys. Rev. Lett. **103**, 147601 (2009).
[67] T. Shibata, Y. Fukuzumi, W. Kobayashi, and Y. Moritomo, Sci. Rep. **5**, 9006 (2015).
[68] E. Rucavado, F. Landucci, M. Döbeli, Q. Jeangros, M. Boccard, A. Hessler-Wyser, C. Ballif, and M. Morales-Masis, Phys. Rev. Mater. **3**, 084608 (2019).
[69] J. G. Smith and D. J. Siegel, Nat. Commun. **11**, 1483 (2020).
[70] V. Lacivita, N. Artrith, and G. Ceder, Chem. Mater. **30**, 7077 (2018).
[71] W. Li and Y. Ando, Phys. Rev. Mater. **4**, 045602 (2020).
[72] H. Tian, T. Wang, F. Zhang, S. Zhao, S. Wan, F. He, and G. Wang, J. Mater. Chem. A **6**, 12816 (2018).
[73] H. Zhang, Y. Huang, H. Ming, G. Cao, W. Zhang, J. Ming, and R. Chen, J. Mater. Chem. A **8**, 1604 (2020).
[74] Q. Cheng, Y. Okamoto, N. Tamura, M. Tsuji, S. Maruyama, and Y. Matsuo, Sci. Rep. **7**, 14782 (2017).
[75] J.-P. Hansen and I. R. McDonald, *Theory of Simple Liquids: With Applications to Soft Matter* (Academic Press, Oxford, 2013).